

Supplement of “On the suitability of the Thorpe-Mason model for Calculating Sublimation of Saltating Snow”

Varun Sharma¹, Francesco Comola¹, and Michael Lehning^{1,2}

¹School of Architecture, Civil and Environmental Engineering, Swiss Federal Institute of Technology, Lausanne, Switzerland

²WSL Institute for Snow and Avalanche Research SLF, Davos, Switzerland

Correspondence: Varun Sharma (varun.sharma@epfl.ch)

Introduction

The contents of this supplement are intended to describe in detail, the numerical methods used in this study, the physical and empirical parameters and constants employed and additional results that complement those presented in the main portion of the article.

5 S1 Large-eddy simulation - equations and numerical setup

S1.1 Flow equations

The large-eddy simulation (LES) technique solves three-dimensional filtered Navier-Stokes (N-S) equations in rotational form for an incompressible flow in hydrostatic equilibrium along with the continuity equation. Advection-diffusion equations for temperature and specific humidity are solved and resulting buoyancy forces are added to the N-S equations using the Boussinesq approximation. The equations solved (presented using Einstein’s convention) are as follows.

$$\partial_t \tilde{u}_i + \tilde{u}_j (\partial_j \tilde{u}_i - \partial_i \tilde{u}_j) = -\frac{1}{\rho_f} \partial_i \tilde{p}_\infty \delta_{i,1} - \frac{1}{\rho_f} \partial_i \tilde{p}^* - \partial_j \tilde{\tau}_{ij} + g \left(\frac{\tilde{\theta}_v - \langle \tilde{\theta}_v \rangle}{\langle \tilde{\theta}_v \rangle} \right) \delta_{i,3} + \frac{1}{\rho_f} S_i^m, \quad (\text{S1})$$

$$\partial_i \tilde{u}_i = 0, \quad (\text{S2})$$

$$\partial_t \tilde{\theta} + \tilde{u}_j \partial_j \tilde{\theta} = -\partial_j \tilde{\pi}_j + \frac{1}{\rho_f c_{p,f}} (S^h), \quad (\text{S3})$$

$$\partial_t \tilde{q} + \tilde{u}_j \partial_j \tilde{q} = -\partial_j \tilde{\Omega}_j + S^q, \quad (\text{S4})$$

$$\tilde{\theta}_v = \tilde{\theta} (1 + 0.61 \tilde{q}). \quad (\text{S5})$$

In the above equations, u_i are the three velocity components, θ and θ_v are the potential and virtual potential temperature respectively and q is the specific humidity. The overhead tildes (\sim) represent quantities filtered via spectral cutoff while the brackets ($\langle \rangle$) represent horizontal averaging. Note that in this study, since we are simulating the atmospheric surface layer,

temperature and potential temperature are considered to be the same. The modified pressure term \tilde{p}^* consists of static pressure (p), filtered kinetic energy ($0.5\tilde{u}_i\tilde{u}_i$) and the trace of the subgrid-scale tensor ($\tau_{kk}/3$). The first term on the R.H.S of Eq. (S1) is the large-scale pressure gradient that is imposed to drive the simulation. Terms $\tilde{\tau}$, $\tilde{\pi}$, $\tilde{\Omega}$ represent the subgrid-scale (SGS) fluxes for momentum, heat and specific humidity respectively. The source/sink terms S_i^m , S^h and S^q are included to incorporate the effect of sublimating particles being transported by the wind on the flow dynamics and thermodynamics. Particles exert drag on the flow and exchange heat and mass due to sublimation/deposition. In accordance with the incompressible assumption, we consider the density of the fluid ρ_f to remain constant. The specific heat capacity of air $c_{p,f}$ is considered to be constant irrespective of the value of specific humidity.

S1.2 SGS model

- 10 The deviatoric part of the SGS flux tensor for momentum is computed using a dynamic Smagorinsky-type model, while the scalar SGS fluxes are related to the momentum fluxes using fixed turbulent Prandtl (Pr) and Schmidt (Sc) numbers. The equations used for SGS fluxes are

$$\tau_{ij} = -2\nu_T \tilde{S}_{ij} = -2c_s^2 \Delta^2 |\tilde{S}| \tilde{S}_{ij}, \quad (S6)$$

$$\pi_j = -\frac{\nu_T}{Pr} \partial_j \tilde{\theta}, \quad (S7)$$

$$15 \quad \Omega_j = -\frac{\nu_T}{Sc} \partial_j \tilde{q}, \quad (S8)$$

where, ν_t is the turbulent viscosity of air which is parametrized using a *Smagorinsky-type eddy-viscosity* approach. In this approach, ν_T is considered to be equal to the product of a length scale $c_s \Delta$ times a velocity scale $c_s \Delta |\tilde{S}_{ij}|$. \tilde{S}_{ij} is symmetric part of the strain rate tensor and $|\tilde{S}_{ij}| = \sqrt{2\tilde{S}_{ij}\tilde{S}_{ij}}$ is the Galilean invariant estimate of \tilde{S}_{ij} . The Smagorinsky coefficient, c_s is estimated dynamically using resolved velocity values through applying the Germano identity along trajectories of lagrangian fluid particles. This approach, known as the *Lagrangian Scale-Dependent Dynamic Smagorinsky (LASD)* SGS model was developed by Bou-Zeid et al. (2005), where detailed derivations and applications for LES can be found.

S1.3 Lower-boundary condition for Eulerian quantities

- For the surface boundary conditions for velocity, a non-slip condition is imposed for the vertical velocity and for the horizontal components of the momentum equation an equivalent shear stress is imposed using the log-law with correction for the presence of particles between the surface and the first grid point based on Shao and Li (1999),

$$\tau_{i,3}(x, y, z_1) = \left[\frac{\sqrt{\hat{u}_1^2 + \hat{u}_2^2}}{\ln(z_1/z_0)} \right]^2 \mathbf{n}_i + \frac{1}{\rho_f} S_i^m(x, y, z_1) z_1, \quad (S9)$$

where i represents the direction in the plane parallel to the surface ($i = 1, 2$), and \mathbf{n}_i is a unitary directional vector defined as: $\mathbf{n}_i = \hat{u}_i / \sqrt{\hat{u}_1^2 + \hat{u}_2^2}$. The shear stress is imposed at $z_1 = \Delta z/2$. Recall that $(1/\rho_f) S_i^m$ is the sink of momentum due to drag forces from the flow-particle interaction. In the case with no particles, the stress term reconciles with the standard log law

whereas in the presence of the particles, the stress at the surface decreases (S_i^m is negative). The $(\hat{\sim})$ operator represents a double filtering operation (at 2Δ grid spacing) on horizontal components of the flow, which is equivalent to a local average. The surface roughness is constant over the entire numerical domain and has a value of $z_0 = 10^{-5}$ m. For the numerical integration of the momentum equation, the vertical derivatives of the horizontal velocity components are also needed. These are parametrised at the first grid point also using Monin-Obukhov similarity theory,

$$\partial_3 \tilde{u}_i(x, y, z_1) = \left(\frac{\sqrt{\tau_{i,3}}}{\kappa z_1} \right) \mathbf{n}_i, \quad (\text{S10})$$

with $\tau = \sqrt{\tau_{1,3}^2 + \tau_{2,3}^2}$ and κ is the von Karman constant = 0.4. The kinematic sensible $(\overline{w'\theta'})$ and latent $(\overline{w'q'})$ heat fluxes are zero.

S1.4 Surface-flow coupling

- 10 Ice grains lying on the surface enter into the overlying, usually turbulent fluid through mechanisms of aerodynamic, rebound and splash entrainment from the surface. These mechanisms and the accompanying models used in this work are described in detail in the following paragraphs. There are some common elements in these models. All particles are assumed to enter the flow at a height of $h_{init} = 4 \langle d_p \rangle$ above the surface. Each of these models provides the number of particles per unit area that enter into the flow, along with the initial conditions for both velocity magnitude and direction for the lagrangian particle.

15 S1.4.1 Aerodynamic entrainment

Initiation of aeolian transport of particles occurs due to entrainment of particles by the fluid when the stress at the surface $\tau_{f,surface}$ increases above a threshold value ($\tau_{threshold}$) and particles from the surface are dislodged to relieve stress at the surface. Bagnold (1941) derived an expression for the threshold stress as

$$\tau_{threshold} = A^2 g \langle d_p \rangle (\rho_p - \rho_f) \quad (\text{S11})$$

- 20 where g is the acceleration due to gravity, $\langle d_p \rangle$ is the mean particle diameter of all particles present on the surface, ρ_p and ρ_f are the density of the particles and the fluid respectively. The coefficient A is an empirical parameter taken to be equal to 0.2 based on wind tunnel experiments of drifting and blowing snow by Clifton et al. (2006).

From each computational grid point on the surface, the number of particles entering the fluid due to aerodynamic entrainment at each time-step can then be computed using the expression of Anderson and Haff (1991) as

$$25 \quad N_{ae} = \frac{C_e}{8\pi \langle d_p \rangle^2} (\tau_{f,surface} - \tau_{threshold}) \Delta x \Delta y \Delta t, \quad (\text{S12})$$

where C_e is an empirically derived constant of proportionality (equal to 1.5, according to Doorschot and Lehning (2002) and Δx and Δy are the grid step sizes in the streamwise and cross-stream directions respectively and Δt is the simulation time-step. Once the number of particles has been calculated, for each particle entrained into the flow, the diameter is sampled from the log-normal distribution of the particle size distribution (characterized by the mean, $\langle d_p \rangle$ and standard deviation, σ_{d_p}). The

particle is initialized at height h_{init} and provided with an initial velocity magnitude sampled from a log-normal distribution characterized by mean velocity of $3.5u_*$ and a standard deviation of $2.5u_*$ (Clifton and Lehning, 2008). The ejection angle is sampled from a lognormal distribution with a mean angle as a function of mean particle diameter as follows (Clifton and Lehning, 2008),

$$5 \quad \langle \alpha_{ae,ejection} \rangle = 75 - 55 \left(1 - \exp \frac{-\langle d_p \rangle}{175 \times 10^{-6}} \right). \quad (S13)$$

Thus, at any given time-step, based on the stress at the wall, the number of particles entering the fluid along with the initial position and velocity can be simulated.

S1.4.2 Rebound and splash entrainment

A particle, once entrained within the turbulent fluid, may impact the bed upon which it may rebound back into the fluid (known as *rebound* entrainment) as well as dislodge particles present in the bed that get entrained into the fluid as well (known as *splash* entrainment).

Consider a particle with diameter d_i that impacts the bed with velocity magnitude v_i at a verticle impact angle of α_i . The probability that the particle shall rebound following impact (P_r) is given by Anderson and Haff (1991)

$$P_r = P_m (1 - e^{-\gamma v_i}) \quad (S14)$$

15 where P_m is the maximum probability that is assumed to be equal to 0.9 for snow (Groot Zwaafink et al., 2011) and γ is a empirical coefficient equal to 2 according to Anderson and Haff (1991). Once the particle rebounds, its velocity must be re-initialized. The rebound velocity magnitude v_r is taken to be half of v_i . The vertical rebound angle (α_r) is sampled from an exponential distribution of mean angle equal to 45° following (Kok and Renno, 2009). The particle is assumed to remain in the same vertical plane before and after the collision for simplicity.

20 As mentioned earlier, the impacting particle may break inter-particle bonds present in the snowbed and dislodge additional particles into the overlying turbulent flow. The number of particles dislodged $N_{splash} = \min(N_E, N_M)$, where,

$$N_E = \frac{(1 - P_r \epsilon_r - \epsilon_f) d_i^3 v_i^2}{2 \langle v \rangle^2 \left(\langle d \rangle + \frac{\sigma_d^2}{\langle d \rangle} \right)^3 \left(1 + r_E \sqrt{5 \left[1 + \left(\frac{\sigma_d}{\langle d \rangle} \right)^2 \right]^9 - 5} \right) + 2\phi}, \quad (S15)$$

$$N_M = \frac{(1 - P_r \mu_r - \mu_f) d_i^3 v_i \cos \alpha_i}{\langle v \rangle \left(\langle d \rangle + \frac{\sigma_d^2}{\langle d \rangle} \right)^3 \left(\langle \cos \alpha \rangle \langle \cos \beta \rangle + r_M \sqrt{\left[1 + \left(\frac{\sigma_d}{\langle d \rangle} \right)^2 \right]^9 - 1} \right)} \quad (S16)$$

In the above equations, P_r is the probability of rebound of the impacting grain, calculated using Eq. (S14); ϵ_f and ϵ_r are the fractions of impact energy lost to the bed due to friction and that retained by the rebounding particle respectively. The corresponding fractions of impact momentum are denoted as μ_f and μ_r respectively. The mean and standard deviation of the ejecta's diameter are represented by $\langle d \rangle$ and σ_d . $\langle v \rangle$ is the mean velocity of the ejecta with α and β being the vertical and

horizontal ejection angles of ejected particles. Cohesion of the snow bed is represented by ϕ . Correlation coefficient between the ejected mass m and velocity v^2 is r_E while r_M is the corresponding correlation coefficient between m and v .

The splashed particles are initialized at a height similar to the aerodynamically entrained particles at the height of h_{init} . The initial velocity magnitude is assumed to follow an exponential distribution with a mean value of $0.25 v_i^{0.3}$. The vertical
5 entrainment angle α is chosen as a random number that is drawn from an exponential distribution with a mean value of 50° . The horizontal splash angle β_n is sampled from a Gaussian distribution with a mean value of the horizontal angle of the impacting particle and a standard deviation of 15° (Nalpanis et al., 1993).

Models for splash entrainment are derived by Comola and Lehning (2017) and similar models have previously been implemented by Groot Zwaafink et al. (2014). Additional references can be found in these works.

10 S1.5 Dynamics of particles in flow

Once the ice grain is entrained within the turbulent flow, its fate is determined by solving the equations of motion. The only forces we included in our calculations are drag forces and gravity. The drag forces are computed by considering the ice grains to be spherical and use well-known bulk parametrizations of drag on a sphere in a turbulent flow (Clift et al., 1978). The equations for motion are as follows

$$15 \quad \frac{du_{p,i}}{dt} = (1 + 0.15 Re_p^{0.687}) \frac{1}{t_p} (\tilde{u}_i + u_{sgs,i} - u_{p,i}) - g\delta_{i,3} , \quad (S17)$$

$$t_p = \rho_p d_p^2 / 18 \rho_f \nu_a , \quad (S18)$$

where, $u_{p,i}$ are the velocity components of the particle, \tilde{u}_i is the filtered velocity solved in Eq. (S1), Re_p is the particle Reynolds number (defined later), ν_a is the kinematic viscosity of air and $u_{sgs,i}$ is the SGS fluid velocity computed along the path of the particle's motion. We use the equation for SGS velocities from Weil et al. (2004) as follow,

$$20 \quad du_{sgs,i} = -f \frac{u_{sgs,i}}{T_f} dt + \frac{1}{2} \left(\frac{1}{\sigma^2} \frac{d\sigma^2}{dt} u_{sgs,i} + \frac{\partial \sigma^2}{\partial x_i} \right) dt + \left(f \frac{2\sigma^2}{T_f} \right)^{1/2} d\xi_i , \quad (S19)$$

where $\sigma^2 = 2e/3$ is the variance of the SGS velocity, which is directly proportional to the SGS turbulence kinetic energy (TKE) e . The fraction of TKE present in subgrid scales is represented by f . $d\xi_i$ is a normally distributed random number with zero mean and a variance of dt . The velocity autocorrelation timescale ($T_f = 2\sigma^2/C_o e$) is used to consider the effect of heavy particles as opposed to purely lagrangian particles without inertia.

25 The mass exchange between the ice grain and the surrounding fluid is driven by the difference between the vapour density at the surface of the particle (which is considered to be saturated) and the vapour density in the fluid at the particle location. We assume that the total density of the fluid ρ_f is constant and thus can directly write the mass balance equation as a function

of specific humidity as follows

$$\begin{aligned}\frac{dm_p}{dt} &= \pi \mathcal{D} d_p \rho_f (\tilde{q} - q_{p,surface}) Sh, \\ q_{p,surface} &= \frac{M_W}{R_u T_p \rho_f} e_{s,a} \exp \left[\frac{L_s M_w}{R_u} \left(\frac{1}{T_f} - \frac{1}{T_p} \right) \right], \\ e_{s,a}(T_f) &= 611.15 \exp \left[\left(23.036 - \frac{T_f - 273.15}{333.7} \right) \left(\frac{T_f - 273.15}{6.67 + T_f} \right) \right].\end{aligned}\tag{S20}$$

- 5 In above equation, m_p is the mass of the particle, \mathcal{D} is the diffusion coefficient of vapour in air, \tilde{q} is the filtered specific humidity computed using Eq. (S4), Sh is the Sherwood number (described later) and $q_{p,surface}$ is the specific humidity at the surface, which is computed using the ideal gas law and the Clasius-Clayperon equation, integrated between the particle surface and the mass-boundary layer. M_W is the molecular weight of water, R_u is the universal gas constant and L_s is the latent heat of sublimation. The saturation vapour pressure with respect to ice, $e_{s,a}$ is computed using the Arden-Buck equation for ice.
- 10 The temperature of the particle evolves according to a balance between the latent heat due to mass exchange and the convective heat transfer between the ice grain and the surrounding fluid and can be expressed as,

$$c_i m_p \frac{dT_p}{dt} = L_s \frac{dm_p}{dt} + \pi \mathcal{K} d_p (\tilde{\theta} - T_p) \mathcal{N}u, \tag{S21}$$

where c_i is the specific heat capacity of ice, \mathcal{K} is the thermal conductivity of the air, $\tilde{\theta}$ is the filtered potential temperature obtained by solving Eq. (S3) and $\mathcal{N}u$ is the Nusselt number.

- 15 The effect of turbulence on momentum, heat and mass transfer is neatly encompassed in three non-dimensional parameters, namely the Reynolds, Nusselt and Sherwood numbers respectively. We use the following expressions to calculate these numbers.

$$Re_p = \frac{d |\mathbf{u}_{rel}|}{\nu_{air}}, \tag{S22}$$

$$\mathcal{N}u = 1.79 + 0.606 Re_p^{1/2} Pr^{1/3}, \tag{S23}$$

$$20 \quad Sh = 1.79 + 0.606 Re_p^{1/2} Sc^{1/3}, \tag{S24}$$

The coupling between the particles and the flow occurs through the source/sink terms in equations for momentum (Eq. (S1), S_m), temperature (Eq. (S3), S^h) and specific humidity (Eq. (S4), S^q). Consider a particle lying at a point within in the fluid. The eight closest points of the LES discretized grid shall necessarily form a cube considering that we use a structured Cartesian grid. The point force due to drag upon the particle is simply extrapolated onto these eight points using inverse distance weighting.

- 25 The total force at any LES grid point is a summation of all such extrapolated forces. If an LES grid point has N_p particles

contributing to the total force at it's location, the source/sink terms can be simply represented as

$$\begin{aligned}
S_i^m &= - \sum_{\beta=1}^{N_p} \frac{w_\beta}{\Delta V} \left(m_p \frac{du_{p,i}}{dt} + \frac{dm_p}{dt} u_{p,i} \right)_\beta, \\
S^h &= - \sum_{\beta=1}^{N_p} \frac{w_\beta}{\Delta V} \left(\pi \mathcal{K} d_p \left(\tilde{\theta} - T_p \right) \mathcal{N}u \right)_\beta, \\
S^q &= - \sum_{\beta=1}^{N_p} \frac{w_\beta}{\Delta V} \frac{1}{\rho_f} \left(\frac{dm_p}{dt} \right)_\beta.
\end{aligned} \tag{S25}$$

- 5 In the above equation, w_β is the weight for the extrapolation operation computed using inverse distance weighting.

S1.6 Numerics

The flow equations (Eq.(S1), (S3) and (S4)) are solved in the Eulerian frame of reference using a pseudo-spectral collocation method in the same fashion as that introduced by Moeng (1984) and Albertson and Parlange (1999). In this approach, the horizontal gradient operations are computed using fourier methods while vertical gradients are computed using second order
10 finite differences. Because of the fourier based methods in both horizontal directions, the domain is fully periodic and no lateral boundary conditions are needed, and hence, the domain size tends to infinity in practical effects. The use of fourier methods is quite useful for SGS modelling is because allows the direct use of spectral cut-off for filtering the flow quantities. The horizontal grid is uniform with equal discretizations in the both the streamwise and cross-stream directions. In the vertical direction we use hyperbolic tangent function based grid stretching. This to insure that there are sufficient grid points within
15 the saltation region. Incompressibility is enforced through a prediction-correction approach where the velocity is marched in time and the poisson equation is used to solve for the dynamic pressure field. To maintain proper consistency in numerics for solving the poisson equation, the vertical grid is staggered to ensure second-order accuracy.

Integration in time is done using a second-order Adams-Bashforth scheme. In addition, the non-linear convective terms are dealised with the 3/2 rule (Canuto et al., 1988). The code is fully parallelised using Message Passing Interface (MPI), and the
20 FFTW library (Frigo and Johnson, 2005) is employed for the Fourier transforms. The pressure solver is based on the pipeline Thomas algorithm (Povitsky and Morris, 2000) and is used to enforce incompressibility implied by Eq. (S2).

The equation of motion for particles (Eq. (S17)) along with equations for heat and mass budgets (Eq. (S20) and (S21)) are solved using a simple first-order time stepping using forward euler method. At each timestep, information from the Eulerian LES grid is translated to locations of the lagrangian particles using simple linear interpolation. The source/sink terms due
25 to the flow-particle coupling are translated back to the Eulerian frame of reference using linear extrapolation as described in Eq. (S25).

All simulations in this study are driven by an imposed large-scale pressure gradient $\mathcal{P} = -(1/\rho_f) \partial \widetilde{p}_\infty / \partial x$ in the stream-wise direction. This quantity is kept constant throughout the simulation. Upon choosing values of the surface friction velocity u_* , the imposed pressure gradient can be computed as $\mathcal{P} = u_*^2 / L_z$, where L_z is the vertical extent of the computational
30 domain.

S2 Physical constants and numerical parameters used in the study

Table S1. Important Physical Parameters and Constants

Parameter	Symbol [Units]	Value
Latent heat of sublimation	L_s [J kg ⁻¹]	2835.49×10^3
Prandtl number	Pr [—]	0.72
Schmidt number	Sc [—]	0.63
Molecular Weight of Water	M_w [kg mol ⁻¹]	0.018015
Density of ice	ρ_p [kg m ⁻³]	918.4
Density of air	ρ_f [kg m ⁻³]	1.34
Specific heat capacity of air	$c_{p,f}$ [J kg ⁻¹ K ⁻¹]	1.005×10^3
Specific heat capacity of ice	c_i [J kg ⁻¹ K ⁻¹]	2.0357×10^3
Roughness length	z_0 [m]	1.0×10^{-5}
Cohesion Strength	ϕ [J]	10^{-10}
Diffusivity of vapor in air	\mathcal{D} [m ² s ⁻¹]	1.96×10^{-5}
Thermal conductivity of air	\mathcal{K} [W m ⁻¹ K ⁻¹]	0.023
Universal Gas Constant	R_u [J mol ⁻¹ K ⁻¹]	8.314
Kinematic Viscosity of air	ν_a [m ² s ⁻¹]	1.24×10^{-5}

Table S2. Details of the numerical setup

Parameter	Symbol [Units]	Value
Streamwise extent of domain	L_x [m]	6.4
Cross-stream extent of domain	L_y [m]	6.4
Vertical extent of domain	L_z [m]	6.4
Grid points in horizontal directions	$\{nx, ny\}$ [—]	64
Grid points in vertical direction	nz [—]	128
Vertical grid stretching	$\{z_{min}, z_{max}\}$ [m]	{0.01, 0.1}
Time step	Δt [μ s]	50
Total time	T [s]	1200

S3 Supplementary results

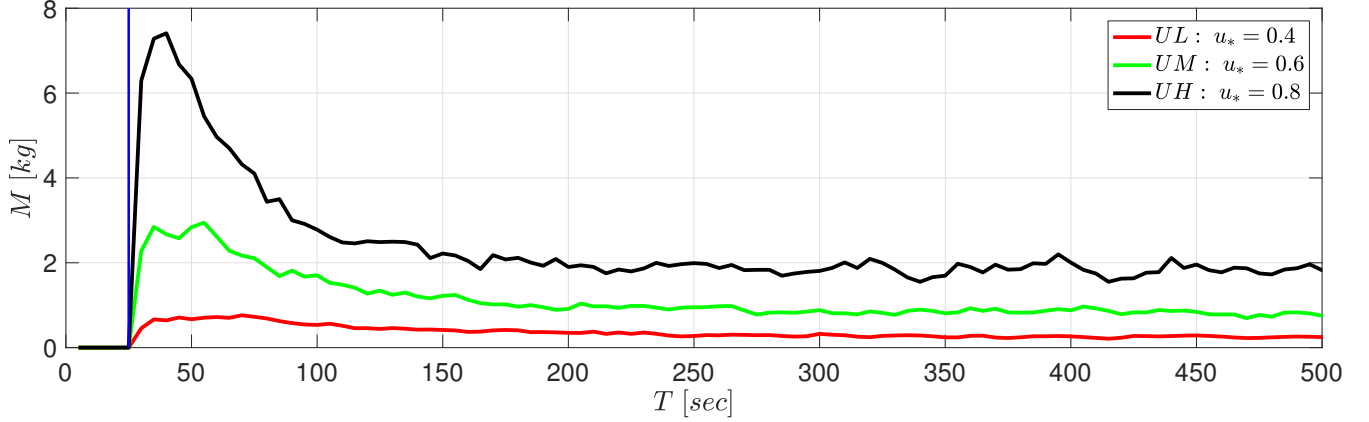


Figure S1. The total mass of snow presented in the fluid at any given time of the simulation for three different forcing conditions. The vertical blue line denotes the commencement of surface erosion.

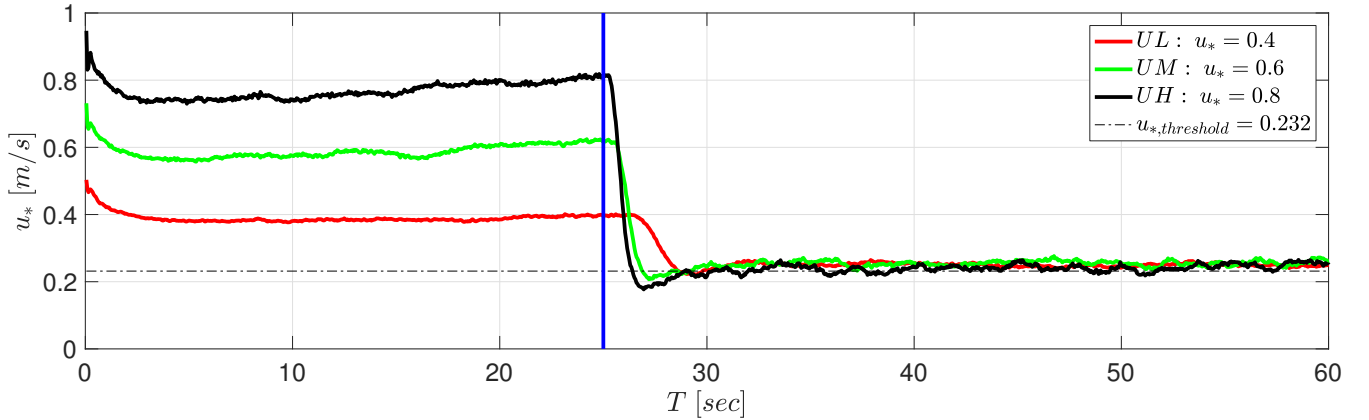


Figure S2. Evolution of the friction velocity at the surface (u_*). The vertical blue line denotes the commencement of surface erosion which until this point in time has been artificially restricted.

We present here two results that supplement the results presented in the main portion of the article. While these results are not critical to discussions presented in the article, they are nevertheless interesting in their own right and help justify certain assumptions used in the simulation setup.

- 5 Fig. S1 shows evolution of the total air-borne mass of snow under three different forcing conditions. It shows that once surface erosion is allowed to occur, there is a rapid increase in the total mass present in the atmosphere, following which, it slowly decays to reach its asymptotic value at approximately 300 seconds. All the three forcings, marked by the three initial u_* values of 0.4 (UL), 0.6 (UM) and 0.8 (UH) show similar behaviour with larger mass entrained by the air with increasing u_*

values as expected. The results in Fig. S1 explain the increase in errors in the mass-loss rate with increasing u_* values between the Nu-TM and TM approaches as discussed in Fig. 3 of the article.

In Fig. S2, the evolution of the surface friction velocity is shown as a function of time. The vertical blue line marks the beginning of surface erosion. It shows that irrespective of the forcing used to drive the flow, once saltation begins, the friction velocity at the surface drops to that of $u_{*,threshold}$. The value of $u_{*,threshold}$, computed using Eq.(S11) for $\tau_{threshold}$ and by considering that $u_{*,threshold} = \sqrt{\tau_{threshold}/\rho_f}$ is found to be equal to 0.232. The rate at which the surface friction velocity decays is dependent on the forcing used with larger forcing decaying more rapidly to the asymptotic value of $u_{*,threshold}$. This result is important since the surface friction velocity dictates the turbulent exchange between the surface and the overlying turbulent fluid. A drop in the surface friction velocity shows during drifting and blowing snow events, the heat and mass transfer between the surface and the atmosphere can be neglected as a first-order approximation and can be modelled using fixed stress values in more detailed studies.

S3.1 Vertical profiles of mean and turbulent quantities

In this section, vertical profiles extracted from the large-eddy simulations in Experiment III are shown to provide additional context for the simulations performed. Note that a detailed analysis of the vertical profiles is out of the scope of the present study and will be presented in a future publication. All the profiles presented below are time-averaged as well as averaged in the horizontal (periodic) directions.

In Fig. S3, the velocity magnitude for the low (UL), medium (UM) and high wind (UH) cases are presented. Influence of initial relative humidity (the RL, RM and RH variants) was not found to be important and thus not presented. Before the snow surface is allowed to be eroded, a fully developed channel flow is allowed to develop. This can be seen in Fig. S2 in the previous section. This also implies the formation of the logarithmic velocity profile as can be seen in Fig. S3. Once the snow surface is allowed to erode, snow transport begins and the particles in the flow cause enhanced drag in the flow. This causes the velocity profile to change with an overall deceleration of the flow. The wind speeds before saltation begins at a height of 1 m above the surface are 11 m/s, 16.33 m/s and 21.86 m/s for the UL, UM and UH cases respectively. Once the snow transport is fully-developed (i.e., when the total mass of snow in the air is constant in Fig. S1), the corresponding wind speeds have reduced to 8.771 m/s (-20%), 11.34 m/s (-30%) and 12.98 m/s (-40%) respectively for the three cases. While reduction of mean wind speed during saltation has been extensively documented for sand transport both in the field, wind tunnel experiments as well as simulations (Bagnold, 1941; Ho et al., 2011; Kok and Renno, 2009), fewer results are available for snow transport. However the available results from Antarctica (Nishimura and Nemoto, 2005), wind tunnels (Clifton and Lehning, 2008) and RANS-type numerical modeling (Nemoto and Nishimura, 2004) are qualitatively similar to those presented here. This is particularly true for the UL and UM cases for which more measurements are available. Most large-scale models account for wind reduction due to saltation by modifying the surface roughness based on empirical laws relating the additional drag due to particles to an effective roughness (Pomeroy et al., 1999). In future work, a comparison of effective surface roughness calculations using different approaches will be made.

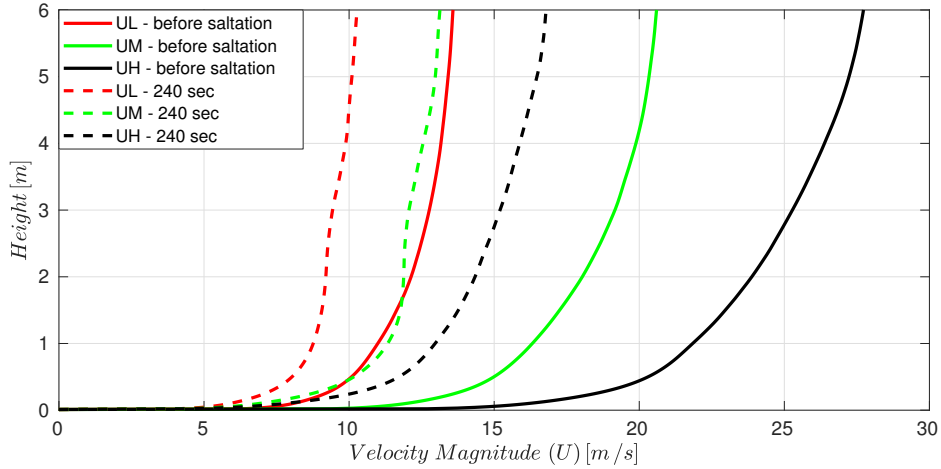


Figure S3. Vertical profiles of mean velocity magnitude for the low (UL), medium (UM) and high wind (UH) cases in Experiment III. For each case, profiles before commencement of saltation and 240 seconds after saltation begins are shown.

The snow drift density is the mass of snow per unit volume present in the air and is shown for the UL-, UM- and UH- cases. Once again, the RL, RM and RH invariants of each of these cases are not found to be significantly different from each other and are thus not presented. Two time points chosen lie during the transient period where increasing snow mass is being entrained into air (profile at 10 seconds) and during fully-developed or steady state snow transport (profile at 240 seconds). The profiles are qualitatively as well as quantitatively (order of magnitude comparison) similar to previous works (see, for example, Gordon et al. (2009)). As expected, the amount of mass in the air increases with increasing wind speed and is found to be concentrated in the lowest 10 centimetres of air above the surface.

Figure S5 presents an inter-comparison of the evolving thermodynamic state of the air computed using either the NUM or the TM approach, with subfigures a,b and c showing vertical profiles of temperature, specific humidity and relative humidity respectively. Only one of the nine cases in Experiment III, namely the UL-RL case is chosen for illustration. Recall that as per our LES setup, the only source or sink of heat and mass in the atmosphere is through interaction with the particles. First, let's focus on subfigure c which shows the relative humidity (R.H) profiles at 3 different times after saltation begins, along with the initial condition for R.H, which in the UL-RL case was fixed at 30% in the entire domain. As time progresses, the R.H in the air increases due to cooling as well as larger amounts of water vapor, both due to sublimation of particles aloft. The profiles on the extreme right of subfigure c, which are extracted 1000 seconds after the start of saltation are similar for both the NUM and TM approaches with the air close to saturation in both the cases. In the profiles at earlier time-steps, the R.H is higher near the surface and decreases with height as expected. The near surface air reaches a high saturation-rate (90%) within 100 seconds after saltation begins, but it takes almost 900 seconds more to reach saturation. This can be explained by turbulent mixing which continuously supplies dry air from aloft to the near-surface region.

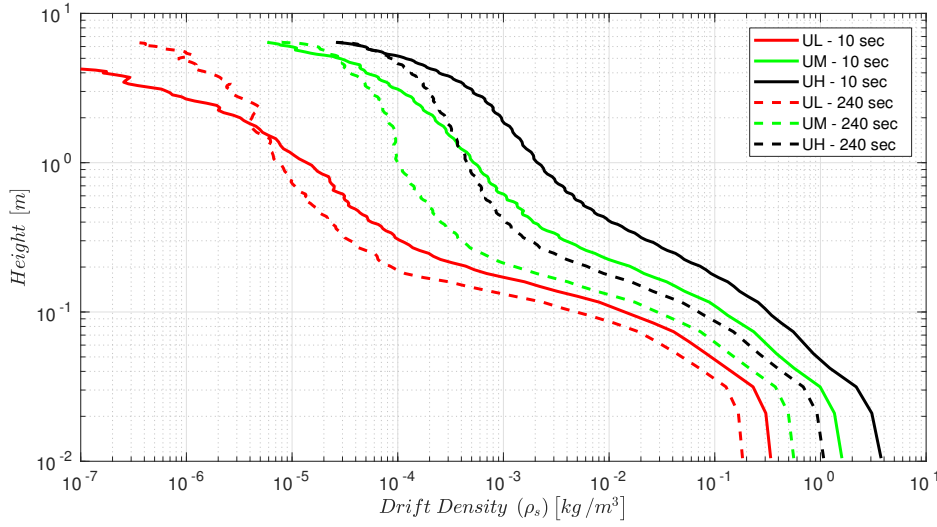


Figure S4. Vertical profiles of snow drift density for the low (UL), medium (UM) and high wind (UH) cases in Experiment III. For each case, profiles 10 seconds and 240 seconds after commencement of saltation are shown.

While Fig. S5c, shows qualitatively a similar behavior for both the NUM and TM approaches as far as R.H evolution is concerned, we have shown in the main text that the TM approach underestimates the mass flux due to sublimation as compared to the NUM approach (see Figure 4 in the main article). The reason for this is the difference in the total cooling of the air between the two cases. This can be observed in the temperature profiles in Fig. S5a. For the TM approach, the cooling is much stronger, with the final temperature being 260.3 K, 2.85 K lower than initial air temperature of 263.15 K. On the other hand, for the final air temperature for NUM approach is 262.4 K, almost 2 K warmer than the TM case. The dynamics of the evolution of air temperature are much more complicated in the NUM case due to the inter-play between the thermodynamics of the air as well as the particles. Further work is needed to establish proper thermodynamic constraints on the coupled air-particle system. Ultimately, the results in Experiment I and II show that even for a solitary ice-grain, the TM approach under-predicts the mass sublimated in comparison to the NUM approach for exactly the same environmental conditions. This is reflected in the profiles of specific humidity in subfigure c. The NUM approach, at each of the three time-steps chosen shows higher flux as compared to the TM approach.

Vertical profiles of streamwise $\left(\sqrt{u'u'}\right)$, cross-stream $\left(\sqrt{v'v'}\right)$ and vertical $\left(\sqrt{w'w'}\right)$ velocity fluctuations are shown in Fig. S6 for the UL-RL case before and during saltation. The TKE is highest near the surface and decreases with distance from the surface. Interestingly, during snow transport, each of the TKE components show a decrease as compared to their respective value before snow transport, upto a height on approximately 2 m above the surface. Above this height, the TKE components actually show an increase.

In the final figure in this section, we compare profiles of vertical buoyancy fluxes $\left(\overline{w'b'} = \left(g/\langle\theta_v\rangle_{xy}\right)\overline{w'\theta'_v}\right)$ from three cases, UL-RL, UL-RM and UL-RH, from Experiment III. The three subfigures show profiles for three different times after

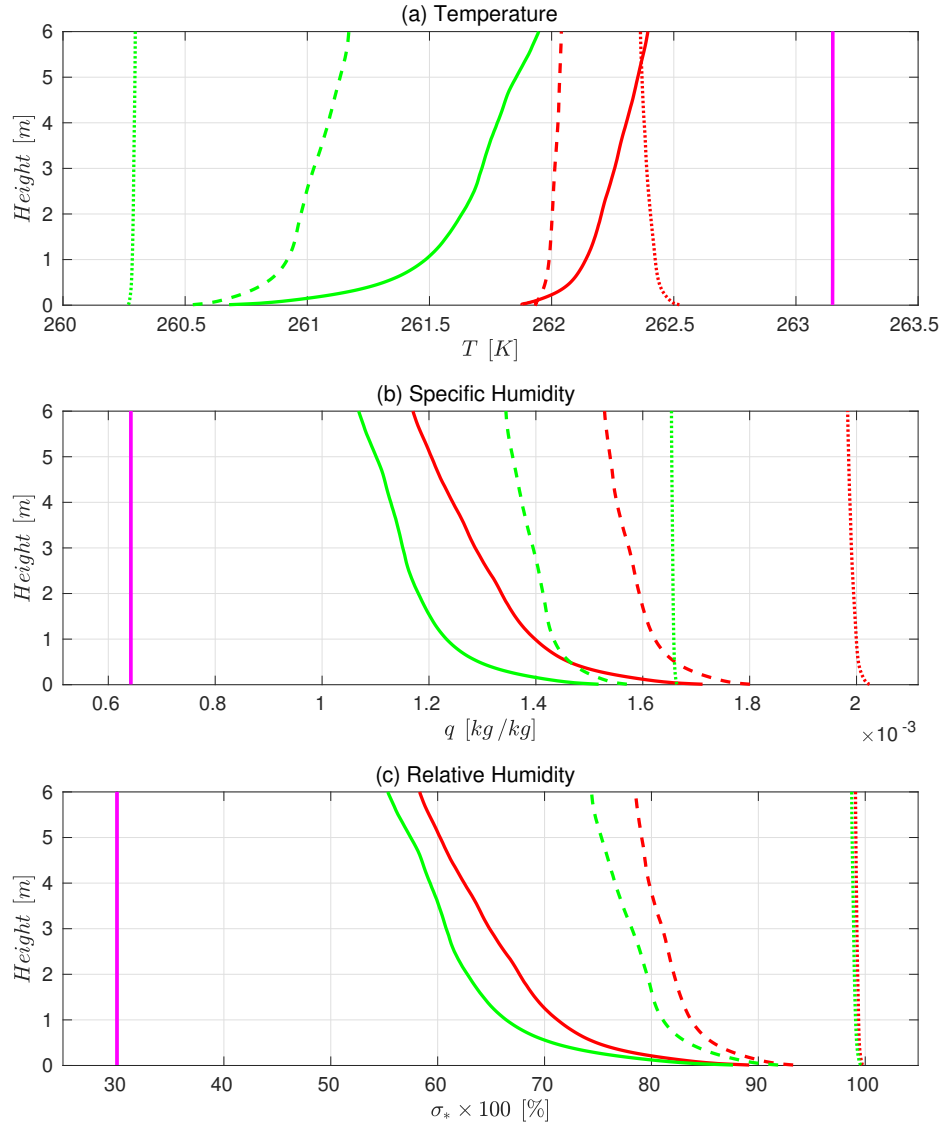


Figure S5. Intercomparison between the NUM (redlines) and TM (green lines) approaches for calculating sublimation of saltating snow in the UL-RL case in Experiment III. The magenta line is the initial condition for temperature, specific humidity and relative humidity. In all the subfigures, the solid, broken and dotted lines are profiles extracted 100, 240 and 1000 seconds after the commencement of saltation respectively.

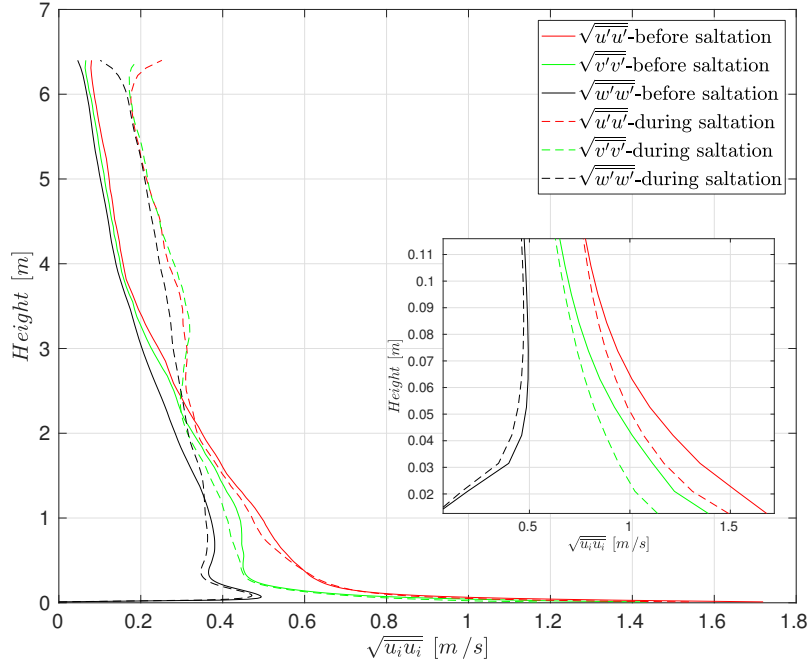


Figure S6. Vertical profiles of the three different constituents of the turbulent kinetic energy before and during saltation (240 seconds after saltation begins) for the case UL-RL in Experiment III.

beginning of saltation. The vertical buoyancy flux is an important quantity as it is a term of the budget equation for vertical velocity fluctuations ($\sqrt{w'w'}$). For each simulation case, the buoyancy flux decreases as time progresses. The UL-RL case is also found to have the largest magnitude of buoyancy flux close to the surface in each of the time-steps shown, followed by UL-RM and finally UL-RH, which has the least buoyancy flux amongst the three cases. Note that this is negative buoyancy flux and thus, in terms of vertical velocity fluctuations, the -RL, -RM and the -RH cases have increasing vertical fluctuations in that order. This could potentially explain the results in Fig. 3a in the main text, where the lighter particles show increasing residence times in the order -RL, -RM and -RH. Further exploration of role of buoyancy in affecting saltation dynamics is left for future work.

S4 Supplementary Movies

- 10 To illustrate the LES simulations performed, two supplementary movies are provided. In Movie M1, saltating particles are shown with the background showing the velocity magnitude. The “blue haze” is the vapor being released from the particles as they sublime in the dry air. The vapor is mixed upwards due to turbulence. In Movie M2, the particles are not shown and the only variable presented is the relative humidity. This movie shows how turbulence brings dry air from aloft towards the surface, resulting in continued sublimation.

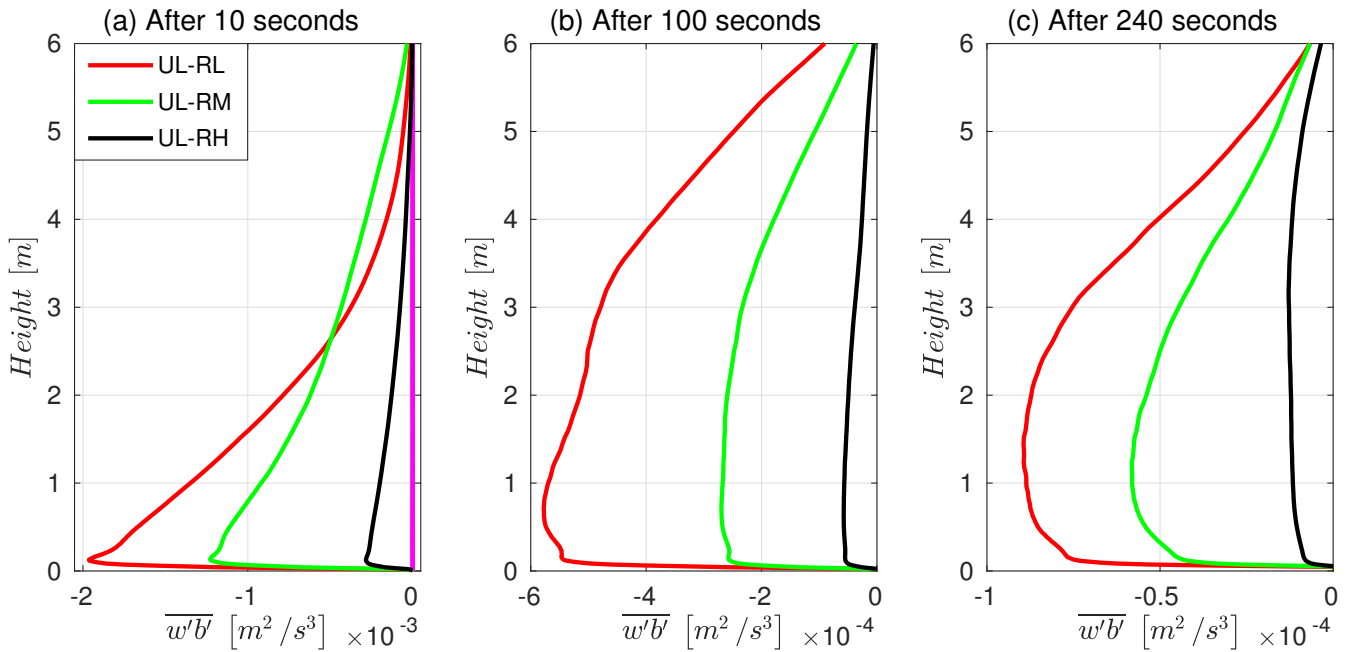


Figure S7. Vertical buoyancy fluxes for three cases, UL-RL, UL-RM, UL-RH at different times after the commencement of saltation.

References

- Albertson, J. and Parlange, M.: Natural integration of scalar fluxes from complex terrain, *Water Resour. Res.*, 23, 239–252, 1999.
- Anderson, R. and Haff, P.: Wind modification and bed response during saltation of sand in air, in: *Aeolian Grain Transport 1*, pp. 21–51, Springer, 1991.
- 5 Bagnold, R. A.: *The physics of blown sand and desert dunes*, New York: Methuen, 1941.
- Bou-Zeid, E., Meneveau, C., and Parlange, M.: A scale-dependent Lagrangian dynamic model for large eddy simulation of complex turbulent flows, *Physics of Fluids*, 17, 025 105, <https://doi.org/10.1063/1.1839152>, <http://dx.doi.org/10.1063/1.1839152>, 2005.
- Canuto, C., Hussaini, M., Quarteroni, A., and Zang, T.: *Spectral Methods in Fluid Dynamics*, Springer-Verlag, Berlin, 1988.
- Clift, R., Grace, J., Weber, M., and Bubbles, D.: *Particles*, Academic, New York, pp. 171–202, 1978.
- 10 Clifton, A. and Lehning, M.: Improvement and validation of a snow saltation model using wind tunnel measurements, *Earth Surface Processes and Landforms*, 33, 2156–2173, <https://doi.org/10.1002/esp.1673>, <https://onlinelibrary.wiley.com/doi/abs/10.1002/esp.1673>, 2008.
- Clifton, A., Rüedi, J.-D., and Lehning, M.: Snow saltation threshold measurements in a drifting-snow wind tunnel, *Journal of Glaciology*, 52, 585–596, 2006.
- Comola, F. and Lehning, M.: Energy- and momentum-conserving model of splash entrainment in sand and snow saltation, *Geophysical Research Letters*, 44, 1601–1609, <https://doi.org/10.1002/2016GL071822>, <http://dx.doi.org/10.1002/2016GL071822>, 2016GL071822, 2017.
- 15 Doorschot, J. J. J. and Lehning, M.: Equilibrium Saltation: Mass Fluxes, Aerodynamic Entrainment, and Dependence on Grain Properties, *Boundary-Layer Meteorology*, 104, 111–130, <https://doi.org/10.1023/A:1015516420286>, <https://doi.org/10.1023/A:1015516420286>, 2002.

- Frigo, M. and Johnson, S.: The design and implementation of FFTW3, *Proceedings of the IEEE*, 93, 216–231, 2005.
- Gordon, M., Savelyev, S., and Taylor, P. A.: Measurements of blowing snow, part II: Mass and number density profiles and saltation height at Franklin Bay, NWT, Canada, *Cold Regions Science and Technology*, 55, 75 – 85, <https://doi.org/10.1016/j.coldregions.2008.07.001>, <http://www.sciencedirect.com/science/article/pii/S0165232X0800102X>, 2009.
- Groot Zwaafink, C. D., Löwe, H., Mott, R., Bavay, M., and Lehning, M.: Drifting snow sublimation: A high-resolution 3-D model with temperature and moisture feedbacks, *Journal of Geophysical Research: Atmospheres*, 116, n/a–n/a, <https://doi.org/10.1029/2011JD015754>, <http://dx.doi.org/10.1029/2011JD015754>, d16107, 2011.
- Groot Zwaafink, C. D., Diebold, M., Horender, S., Overney, J., Lieberherr, G., Parlange, M. B., and Lehning, M.: Modelling Small-Scale Drifting Snow with a Lagrangian Stochastic Model Based on Large-Eddy Simulations, *Boundary-Layer Meteorology*, 153, 117–139, <https://doi.org/10.1007/s10546-014-9934-2>, <https://doi.org/10.1007/s10546-014-9934-2>, 2014.
- Ho, T. D., Valance, A., Dupont, P., and Ould El Moctar, A.: Scaling Laws in Aeolian Sand Transport, *Phys. Rev. Lett.*, 106, 094501, <https://doi.org/10.1103/PhysRevLett.106.094501>, <https://link.aps.org/doi/10.1103/PhysRevLett.106.094501>, 2011.
- Kok, J. F. and Renno, N. O.: A comprehensive numerical model of steady state saltation (COMSALT), *Journal of Geophysical Research: Atmospheres*, 114, n/a–n/a, <https://doi.org/10.1029/2009JD011702>, <http://dx.doi.org/10.1029/2009JD011702>, d17204, 2009.
- Moeng, C. H.: A large-eddy simulation model for the study of planetary boundary-layer turbulence., *J. Atmos. Sci.*, 41, 1984.
- Nalpanis, P., Hunt, J. C. R., and Barrett, C. F.: Saltating particles over flat beds, *Journal of Fluid Mechanics*, 251, 661–685, <https://doi.org/10.1017/S0022112093003568>, 1993.
- Nemoto, M. and Nishimura, K.: Numerical simulation of snow saltation and suspension in a turbulent boundary layer, *Journal of Geophysical Research: Atmospheres*, 109, 2004.
- Nishimura, K. and Nemoto, M.: Blowing snow at Mizuho station, Antarctica, *Philosophical Transactions of the Royal Society of London A: Mathematical, Physical and Engineering Sciences*, 363, 1647–1662, 2005.
- Pomeroy, J. W., Hedstrom, N., and Parviainen, J.: The Snow Mass Balance of Wolf Creek , Yukon : Effects of Snow Sublimation and Redistribution, *Wolf Creek Research Basin: Hydrology, Ecology, Environment.*, pp. 15–30, 1999.
- Povitsky, A. and Morris, P. J.: A higher-order compact method in space and time based on parallel implementation of the Thomas algorithm, *J. Comput. Phys.*, 161, 182–203, 2000.
- Shao, Y. and Li, A.: Numerical Modelling of Saltation in the Atmospheric Surface Layer, *Boundary-Layer Meteorology*, 91, 199–225, <https://doi.org/10.1023/A:1001816013475>, <https://doi.org/10.1023/A:1001816013475>, 1999.
- Weil, J. C., Sullivan, P. P., and Moeng, C.-H.: The Use of Large-Eddy Simulations in Lagrangian Particle Dispersion Models, *Journal of the Atmospheric Sciences*, 61, 2877–2887, <https://doi.org/10.1175/JAS-3302.1>, <https://doi.org/10.1175/JAS-3302.1>, 2004.